Soft Matter

Accepted Manuscript

ROYAL SOCIETY OF CHEMISTRY

www.rsc.org/softmatter

Mechanically Programmed Shape Change in Laminated Elastomeric Composites

Jaimee M. Robertson[a,b], Amir H. Torbati[a,b], Erika D. Rodriguez[a,b], Yiqi Mao[c], Richard M. Baker[b], H. Jerry Qi[c], and Patrick T. Mather[b]*

Received (in XXX, XXX) Xth XXXXXXXXX 20XX, Accepted Xth XXXXXXXXX 20XX
DOI: 10.1039/b000000x

Keywords: anisotropy, elastomeric composites, mechanical programming, modeling, shape memory polymers

Abstract:

Soft, anisotropic materials, such as myocardium in the heart and the extracellular matrix surrounding cells, are commonly found in nature. This anisotropy leads to specialized responses and is imperative to material functionality, yet few soft materials exhibitting similar anisotropy have been developed. Our group introduced an anisotropic shape memory elastomeric composite (A-SMEC) composed of non-woven, aligned polymer fibers embedded in an elastomeric matrix. The composite exhibited shape memory (SM) behavior with significant anisotropy in room-temperature shape fixing. Here, we exploit this anisotropy by bonding together laminates with oblique aniostropy such that tensile deformation at room temperature – mechanical programming – results in coiling. This response is a breakthrough in mechanical programming, since non-affine shape change is achieved by simply stretching the layered A-SMECs at room temperature. We will show that pitch and curvature of curled geometries depend on fiber orientations and the degree of strain programmed into the material. To validate experimental results, a model was developed that captures the viscoplastic response of A-SMECs. Theoretical results correlated well with experimental data, supporting our conclusions and ensuring attainability of predictable curling geometries. We envision these smart, soft, shape changing materials will have aerospace and medical applications.

Introduction

Shape memory polymers (SMPs) have the ability to "memorize" a permanent shape. After deformation to a fixed temporary shape, SMPs are capable of recovering to their permanent form upon application of an external stimulus such as water,[1] light,[2] force, or heat.[3-5] Applications of these polymers are vast, and many have been developed for actuators, medical devices, smart adhesives, and sensors.[6] However, very few studies focused on mechanically programmed SMPs, where force is used to initiate shape change. As will be explained in this paper, achieving a mechanically programmed SMP is possible via the fabrication of an anisotropic elastomeric composite.

In the context of SMPs, soft and anisotropic materials can play a vital role in the field of biomaterials.[7-9] Most fabricated elastomeric materials are isotropic while there is a need for elastomeric materials that mimic the anisotropic properties observed in nature in materials such as tendons,[10] wood, or bat wings. Further, the extracellular matrix found in the human body is comprised of Type III collagen and elastin small diameter fibers arranged in an anisotropic manner.[11] Another example is myocardium in heart muscle tissue.[12] Indeed, researchers have tried to replicate the cardiac anisotropy synthetically.[13-15] Engelmayr et al. synthesized an anisotropic elastomeric scaffold using poly(glycerol sebacate) and demonstrated the development of cell alignment using this material. Plants are also among the biological systems that demonstrate anisotropy. *Passiflora edulis*, for example, have long, curly tendrils that form both spirals and helices. This behavior was modeled using synthetic liquid crystalline cellulosic fibers.[16] The curling of such materials with complex geometries can be quantified by measuring the pitch and radius of curvature. Armon et al. used these parameters to describe the geometry of opened *Bauhinia variegate* seed pods.[17] This type of seed has valves composed of two fibrous layers, with fiber orientations at ±45° with respect to the longitudinal direction of the pod. Opening of the pods is triggered by shrinkage due to changes in humidity. As the valves shrink, curling is observed due to differences in the

recovery direction between the two layers. The difference in recovery directions is a result of the anisotropy of the aligned fiber layers. Studying and understanding these anisotropic biological materials helps scientists to fabricate smart biomaterials for biomedical applications. In recent years, anisotropic polymers,[7, 18] anisotropic liquid crystalline elastomers,[8, 19] and anisotropic elastomeric composites[9] with shape memory (SM) properties have been studied. The latter were developed by our group and were utilized in the current work. Therefore, significant design details and results from the previous study are subsequently described.

Composite polymeric materials can be used to create SMPs that are elastomeric in the desired temperature range. The anisotropic SM elastomeric composite (A-SMEC) recently introduced by our group was constructed through electrospinning aligned fibers of poly(vinyl acetate) (PVAc) and infiltrating Sylgard 184 silicone into the fiber mat.[9] While Sylgard 184 is capable of "memorizing" a permanent shape, it lacks the ability to fix a temporary shape when in the elastomeric state. To enable shape fixing in the elastomer, the PVAc fibers were introduced; the PVAc served as the SM fixing polymer and Sylgard 184 served as the soft matrix assisting in SM recovery. This combination allowed for an overall elastomeric behavior of the composite material.[9] The fiber mat was fabricated to be anisotropic, with its mechanical properties being dependent on the fiber direction. Specifically, the Young's modulus, a measure of material stiffness, depended strongly on fiber direction. This anisotropy translated to the composite, and it was demonstrated that the ability to fix a temporary shape depended on the PVAc fiber orientation in the A-SMEC. When the composite material was stretched in the direction of the polymer fibers, as opposed to the direction perpendicular to the fiber orientation, for example, a higher fixing ratio was attained.

For the present study, we introduce a new concept of mechanically programming complex temporary shapes into SMPs while dramatically simplifying the SM cycle and simultaneously introducing a significant technical challenge of accurate shape prescription.

From our prior study, we postulated that a stack of A-SMECs with distinct fiber angles in each layer would feature a gradient in shape-fixing through the thickness. This gradient was further expected to cause a non-affine shape change, for example curling of a bilayer toward the side with less fixing. This transformation from 2D to 3D would be remarkable, considering that its programming requires solely uni-axial tensile deformation without heating; i.e., obviating the time consuming heating/deform/cool sequence of standard shape memory programming. While similar shape changes have been obtained previously, there are several advantages to the current approach that make it more suitable for a range of applications.[20-21] For example, Jeong et al. developed a layered composite system that selectively swells in response to solvent polarity.[20] Through manipulation of the layered geometry, helices were formed upon solvent exposure. Limitations to this approach include the maintenence of the solvent environment and the long time scale required to reverse the shape change. Similarly, Kohlmeyer et al. chemically modified Nafion strips to from helices in response to a change in temperature.[21] While the thermal environment need not be maintained, significant changes in pH are required to enable and reverse the shape change. Furthermore, the Nafion strip must undergo a typical shape memory cycle prior to chemical modification, making the overall process more labor intensive. Here, we study such curling phenemona, demonstrating control over shape change through the relative angle of ply orientations. Both sample preparation and activation of the shape changing mechanism are simple; tensile deformation triggers the formation of helical structures and heating reverses the shape change. We subsequently characterize the curling and provide a quantitative understanding through the introduction of a mechanical model that predicts the key characteristics of the programmed shape, such as curvature and pitch.

Materials and Methods

Materials

Poly(vinyl acetate) (PVAc) (Mw = 260,000 g/mol) was purchased from Scientific Polymer Products, Inc. N,N-Dimethylformamide (anhydrous, 99.8) (DMF) was purchased from Sigma Aldrich. Methanol was purchased and used as received from Fisher Scientific. Poly(dimethylsiloxane) (Sylgard 184) was purchased from Dow Corning and stored in a refrigerator prior to use.

Electrospinning Method for Fabrication of Anisotropic PVAc Fibers

For sample preparation, two grams of PVAc were dissolved in 10 mL of a 7:3 volume ratio methanol-dimethylformamide mixture to achieve a 20 wt-% poly(vinyl acetate) (PVAc) (260k MW) solution. The solution was electrospun using the setup shown in **Figure 1**.

Electrospinning is the process of applying a voltage to a liquid in order to withdraw thin fibers.[22] A polymer solution in a syringe can be electrospun by applying the voltage to the metallic needle. Due to electrostatic repulsion, a cone forms at the tip of the needle, and a jet of solution is shot away from the syringe towards a grounded collector. The resulting fibers are typically collected at random orientations. By introducing a charged copper plate with the plate face perpendicular to the syringe needle, the direction of the jet can be influenced. The metal plate creates a more uniform electric field, producing fiber mats with aligned fibers.

In order to electrospin the aligned fibers, the PVAc solution was pumped at 0.5 mL h^{-1}. A voltage of +14 kV was applied to the syringe needle, and a voltage of +12 kV was applied to the copper plate. The grounded metal collector drum (-0.5 kV) rotated at 3000 rpm, and the distance between the needle tip and the collector drum was 8 cm. Electrospinning was run for 8-10 h. After removing, the fiber mat was dried in a vacuum oven at RT for 24 h.

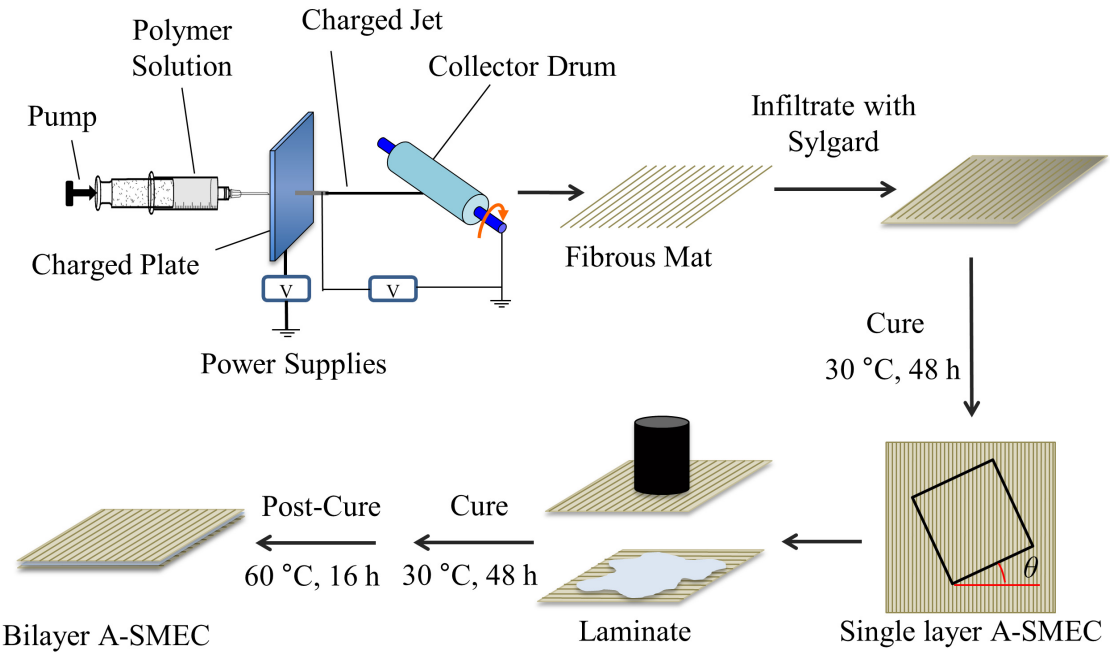

Figure 1. Fabrication of single layer and bilayer anisotropic shape memory elastomeric composites (A-SMEC). Aligned PVAc fibers were electrospun and subsequently infiltrated with Sylgard to form the single layer A-SMECs. Square sections with various fiber orientations (θ) were adhered with a layer of Sylgard between them to form the bilayer A-SMECs.

Anisotropic Single Layer Composite Fabrication

An elastomeric composite was prepared by applying a 10:1 mass ratio base:curing agent of a two-part Sylgard 184 (hereafter "Sylgard") mixture. The Sylgard was applied to one side of the fiber mat with a spatula, and a heavy roller was used to remove excess Sylgard and evenly distribute the mixture. The fiber mat was turned over, and the process was repeated. The infiltrated fiber mat was put into a vacuum oven (ca. 760 mm Hg) at RT for 1 h to assist the fiber infiltration and to remove air bubbles from the Sylgard. After removal from the vacuum oven, the composite material was cured at 30 °C for 48 h.

Anisotropic Bilayer Composite Fabrication

Squares (30 mm in length) were cut from the anisotropic single layer composite at various fiber angles (θ = 0°, 22.5°, 45°, 67.5°, and 90°). The reported angles are indicative of the

angle between the direction of the fibers and the cutting direction in the PVAc fiber mats. Two plies were stacked and adhered with Sylgard, and excess Syglard was removed by running a heavy roller over the top layer. The prepared bilayers had layers with fiber angles of 0°/0°, 0°/22.5°, 0°/45°, 0°/67.5°, and 0°/90° (top fiber orientation-bottom fiber orientation). Since each prepared bilayer had one layer with 0° orientation, we will hereafter use the term "Δθ" which refers to the difference in fiber angle between the two layers (Δθ = 0°, 22.5°, 45°, 67.5°, and 90°). A schematic of this layering process is shown in **Figure 1**. The bilayers were put in a vacuum oven (ca. 760 mm Hg) at RT for 1 h to remove air bubbles from the Sylgard layer in between the two plies. After removing, the bilayers were cured at 30 °C for 48 h and then post cured at 60 °C for 16 h to ensure that the Sylgard crosslinking was complete. Based on measurements from 5 samples, the Sylgard thickness adhering the two lamina was calculated to be less than 16% of the overall thicknesses of the bilayer A-SMECs in all cases.

Scanning Electron Microscopy

A JEOL JSM-5600 Scanning Electron Microscope (SEM) was used to study the microstructural morphology and topography of the anisotropic composites. SEM was performed on the PVAc fiber mats, single layer A-SMECs, and bilayer A-SMECs. All samples were sputter coated with gold for 45 s prior to the SEM analysis. SEM micrographs of the surface of the electrospun aligned PVAc fiber mats were taken in order to verify fiber alignment. The surface and the transverse and longitudinal cross-sections of the infiltrated fiber mat and the bilayer composite were also visualized. SEM micrographs of the bilayer cross-sections were used to measure the thickness of the Sylgard layer that was used to adhere the two plies. All micrographs were obtained using an accelerating voltage of 8 – 10 kV. ImageJ software (Version 1.46) was used for PVAc fiber diameter measurements.

Thermal Analysis

Thermal properties of samples were characterized using Differential Scanning Calorimetry (DSC); (Q200 TA Instrument). Samples were heated from -60 °C to 160 °C to remove the thermal history, cooled to -60 °C, and finally heated to 160 °C at the rate of 10 °C min^{-1} to determine the glass transition (T_g) temperatures. The DSC cell was purged with nitrogen gas at 50 mL min^{-1} to ensure an inert, dry, and reproducible environment. The second cooling and heating were studied and reported. DSC was performed on PVAc fiber mats, neat Sylgard, and the bilayer A-SMECs in order to measure the transition temperatures. DSC of the single layer A-SMECs was studied in our previous work.[9]

Mechanical Testing

To calculate the Young's modulus of the PVAc fiber mats and the single and bilayer A-SMECs, dog-bones (ASTM D638-10), with a gauge length of 6.25 mm and width of 1.5 mm, were cut from the samples. The dog-bones from the PVAc fiber mats and single layer A-SMECs were cut with $\theta = 0°$, 22.5°, 45°, 67.5°, and 90°; and the dog-bones were cut from the bilayer A-SMECs with $\Delta\theta = 0°$, 22.5°, 45°, 67.5°, and 90°. These angles correspond to the angle between the direction parallel to the fibers and the loading direction. At 25 °C, the samples were stretched at 33 μm s^{-1} until failure using a Linkam TST 350 tensile stress testing system equipped with a 20 N load cell. The Linkam system measures the force required to stretch the sample and the distance the sample has been stretched, which were converted to engineering stress and strain, respectively. In addition, the Young's modulus was computed from the slope of the stress-strain curve in the linear, elastic region. Typical sample thicknesses ranged from 0.08-0.12, 0.2-0.3, and 0.4-0.6 mm for the PVAc fiber mats, single layer A-SMECs, and bilayer A-SMECs, respectively.

Reversible Plasticity Shape Memory

Reversible plasticity SM (RPSM) of single layer A-SMECs was quantified using a Q800 TA Dynamic Mechanical Analyzer (DMA). A RPSM method was developed to describe the reversal of elastic and plastic deformation upon a thermal stimulus. Here, the so called reversible plasticity of the A-SMEC is based on the observation that the PVAc can develop significant plastic deformation at low temperatures. Such deformation provides the shape fixing capability, but the recovery force of the elastomeric matrix can recover this plastic deformation when the PVAc is heated above its T_g and is capable of flowing easily. This method helps to understand and compare the fixing and recovery ratios of each single layer A-SMEC with different θ relative to the direction of stretching at RT. Prior to testing, thermal history of the samples were removed by heating to 60 °C for 20 min, followed by cooling to RT for 5 min. Dog-bone specimens were cut at different θ using a dog-bone die. For this experiment, DMA was set to controlled force method in a tensile mode. A preload force of 0.001 N was used, and the sample was first equilibrated at 25 °C. After being held isothermal for 3 min, the sample was set to be stretched to 75% strain by ramping the force at 0.02 N min^{-1} (Step 1). In the stretched state, the sample was held isothermal for 1 min and then the force was ramped to 0.001 N at a rate of 0.05 N min^{-1} for unloading (Step 2). The sample was again held isothermal for 1 min, after which the temperature was ramped at 2 °C min^{-1} to 60 °C for shape recovery (Step 3). At 60 °C, the sample was held isothermal for 3 min to allow time for shape recovery. The temperature was then ramped at 2 °C min^{-1} to 25 °C to complete the first SM cycle (Step 4). All steps were repeated two more times for a total of 3 RPSM cycles, and a minimum of 3 samples with each fiber orientation were tested. The degree of fixing (R_f) and degree of shape recovery (R_r) were calculated for each cycle based on the following equations:

$$R_f(\%) = \left(\frac{\varepsilon_{fixed}}{\varepsilon_{deformed}} \right) \times 100 \quad (1)$$

$$R_r(\%) = \left(\frac{\varepsilon_{fixed} - \varepsilon_{recovered}}{\varepsilon_{fixed} - \varepsilon_{initial}} \right) \times 100 \quad (2)$$

where $\varepsilon_{deformed}$ is the maximum strain after deformation at RT, ε_{fixed} is the strain upon unloading at RT, $\varepsilon_{recovered}$ is the strain recovered after heating, and $\varepsilon_{initial}$ is the initial strain at the beginning of each cycle.

Curvature and Pitch Analysis of Mechanically Programmed Shape Change

In order to determine the relationship between fiber orientation and the curling phenomenon, 30 (l) x 2.5 (w) mm rectangular strips were cut from the bilayer A-SMECs. Typical sample thicknesses were between 0.6 and 0.7 mm. Using the Linkam system, the rectangular strips were stretched at a rate of 33 μm s^{-1} at 25 °C to strains of 40%, 50%, 75%, and 100%. These strains were chosen to study the breadth of curvature. After reaching the desired strain, each specimen was unclamped, and curling was observed. Images of the curled specimens were taken for further analysis.

To quantify the curling of the bilayers, pitch and radius of curvature were measured. Image J (Version 1.46) was used to obtain quantitative measurements for the pitch and radius of curvature. The pitch was obtained by measuring the distance between consecutive peaks or troughs of the curled sample, and the radius of curvature was obtained by measuring the diameter of the sample in its curled state and dividing by 2.

Modeling of Curvature

To simulate the anisotropic viscoplastic behavior of the mechanically programmed A-SMECs, a simple model was developed. Consider a bilayer A-SMEC stretched uni-axially as depicted in **Scheme 1a**. According to the classical Euler-Bernoulli theory, the normal strain along the x-direction is defined as[23]

$$\varepsilon_1(z) = \varepsilon_0 + \kappa \cdot z \tag{3}$$

where κ is the curvature and z is the distance from the neutral axis. This can be rewritten in incremental form as

$$\Delta\varepsilon_1(z) = \Delta\varepsilon_0 + \Delta\kappa \cdot z \tag{4}$$

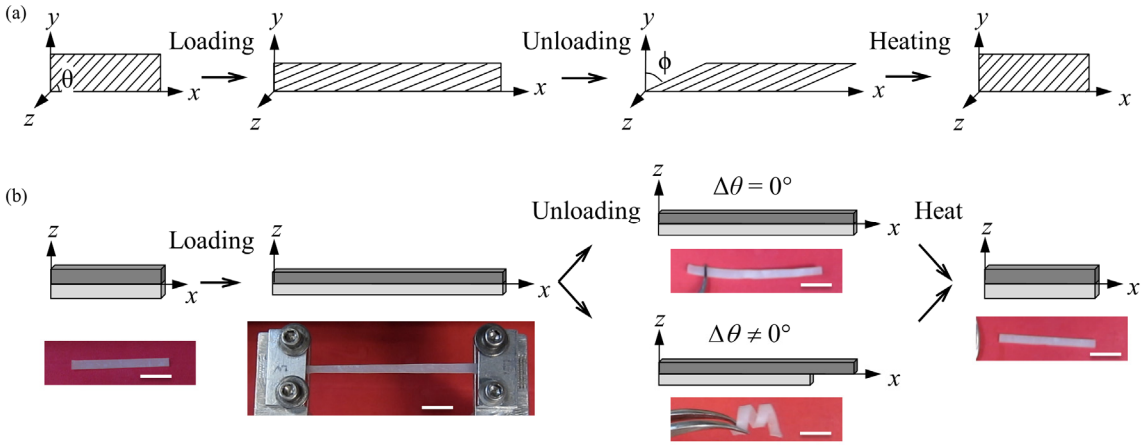

Scheme 1. (a) Diagram showing the effect of stretching a single layer A-SMEC. The angles θ and ϕ are indicated and represent the fiber angle and the in-plane rotation angle, respectively. (b) Diagram showing the effect of stretching a bilayer A-SMEC. Upon unloading, the fixing mismatch in bilayer A-SMECs leads to the curvature phenomenon. There is no mismatch between the layers for Δθ = 0° which leads to a straight sample post stretching. Alternatively, different curvatures are observed for Δθ ≠ 0° due to the mismatch between the layers. The curled sample in (b) had Δθ = 45°. Upon heating, all samples return to their original shape. Scale bars represent 5 mm.

To consider the in-plane rotation of the bilayer upon unloading, equilibrium of in-plane shear stress should be applied. We introduce the angle, ϕ, to depict the in-plane rotation angle as shown in **Scheme 1a**. The pitch of the helices in the unloaded bilayer can be calculated for a given the radius of curvature, R as follows

$$H_{pitch} = 2\pi R\gamma\,, \tag{5}$$

where $\gamma = \tan\phi$ is the shear deformation. For the constitutive relation of A-SMECs, it is considered to be a combination of two parts, Sylgard matrix and PVAc fiber. The matrix behaves as an entropic elastomer while the PVAc fiber behaves as a nonlinear solid. A standard linear solid model is applied to capture the viscous property of the PVAc fibers.

Therefore, the total constitutive relation of A-SMECs along the axial direction is defined in terms of axial stretch, λ_1, as follows

$$\sigma_1 = \underbrace{E_m\left(\lambda_1^2+\gamma^2\right)}_{\sigma_m} + \underbrace{E_f\left(\lambda_1\cos\theta+\gamma\sin\theta\right)^2}_{\sigma_{f_{eq}}} + \underbrace{2E_f\beta\cos\theta\left(\lambda_1\cos\theta+\gamma\sin\theta\right)\int_0^t\dot{\lambda}_1(s)\exp\left(-\frac{t-s}{\tau(T)}\right)\mathrm{d}s}_{\sigma_{f_{neq}}} \tag{6}$$

where E_m is the matrix modulus, E_f is the fiber modulus, θ is the fiber orientation angle, T is temperature, τ is the relaxation time of the fibers, β is a parameter that characterizes the influence of the interface on the nonequilibrium stress, and s is the shear flow resistance, and is introduced to depict shear deformation. The matrix modulus and fiber modulus can be determined as follows

$$E_m = Nk_BT \tag{7}$$

$$E_F = \frac{1}{3}\mu_F\left(\lambda_F{}^2-1\right) \tag{8}$$

where N is crosslinking density, k_B is Boltzmann's constant, μ_f is the fiber shear modulus, and λ_F is the fiber stretch, for which a detailed definition is given in the Supporting Information. The anisotropic property of A-SMECs provided by the oriented reinforcing fibers is reflected in the fiber modulus and the dependence of fiber modulus on fiber orientation angle.

In addition, upon unloading, the bilayer structure will twist due to the anisotropy of the material. Therefore, equilibrium of in-plane shear stress should be considered, and the shear constitutive relation is defined as

$$\sigma_{12} = E_M\left(\lambda_1^{-1/2}\gamma\right) + E_F\left(\lambda_1^{1/2}\sin\alpha\cos\alpha+\lambda_1^{-1/2}\gamma\left(\sin\alpha\right)^2\right) \tag{9}$$

For the shear constitutive relation, no explicit shear viscoelastic deformation is considered for simplicity. To capture the temperature dependence and stretch softening/strengthening of PVAc, the relaxation time in Eq. 6 is defined as[24]

$$\tau = \tau_0 \alpha_T(T) \exp\left(-\frac{\Delta G}{k_B T}\frac{\sigma_e}{s}\right) \tag{10}$$

where, $\alpha_T(T)$ is the time-temperature superposition (TTSP) shift factor, τ_0 is the relaxation time at the reference temperature when $\alpha_T(T)=1$, and ΔG is the zero-stress level activation energy. At temperatures above T_s the Williams-Landel-Ferry (WLF) equation[25] is used:

$$\log \alpha(T) = -\frac{C_1\left(T-T_M\right)}{C_2+\left(T-T_M\right)} \tag{11}$$

where C_1 and C_2 are material constants and T_M is the WLF reference temperature. As for temperatures below T_s, the temperature shift factor $\alpha(T)$ is set to follow the Arrhenius-type behavior[26] as:

$$\ln \alpha(T) = -\frac{AF_c}{k_B}\left(\frac{1}{T}-\frac{1}{T_g}\right) \tag{12}$$

The constitutive relation equations for axial and shear stress were solved incrementally, the details of which are available in the Supporting Information.

At each time step, the strain increment and curvature increment can be calculated using Eq. S14 with boundary conditions (Eq. S15 or S16), and the total strain and curvature at the current step can be obtained as

$$\varepsilon_0^{n+1} = \varepsilon_0^{n} + \Delta\varepsilon_0^{n+1}, \tag{13a}$$

$$\kappa^{n+1} = \kappa^{n} + \Delta\kappa^{n+1}, \tag{13b}$$

$$\gamma^{n+1} = \gamma^{n} + \Delta\gamma^{n}. \tag{13c}$$

For comparison, the radius of curvature and curvature are normalized as

$$R_{norm} = \frac{1}{\kappa(h_1 + h_2)}, \quad \kappa_{norm} = \frac{1}{R_{norm}} \tag{14}$$

where h_1 and h_2 are the thicknesses of layer 1 and layer 2, respectively. In doing this, there are two main assumptions. The first is that the layer of Sylgard that adheres the two infiltrated layers together is of negligible thickness. This is a reasonable assumption because the thickness added by the layer of Sylgard is less than 16% of the total thicknesses of the bilayer A-SMEC. The second assumption is that the thickness of each layer of the bilayer A-SMECs is equal to half of the total thickness. Again, this is reasonable assumption because when preparing the bilayers, infiltrated fiber mats of similar thicknesses were matched. The resulting measured normalized curvature values were compared to the predicted normalized curvature values from Eq. 14. With the obtained curvature and shear deformation, the pitch can be calculated using Eq. 5 and the relation, $\phi = \arctan(\gamma)$.

Results and Discussion

Anisotropic PVAc fiber mats, single layer A-SMECs, and bilayer A-SMECs at different fiber angles were fabricated using the method prescribed in the Experimental Section and shown in **Figure 1**. Fiber mat and single layer A-SMECs were tested at various fiber orientations (θ = 0°, 22.5°, 45°, 67.5°, and 90°). Similarly, the prepared bilayer A-SMECs contained layers with fiber angles of 0°/0°, 0°/22.5°, 0°/45°, 0°/67.5°, and 0°/90° (top fiber orientation/bottom fiber orientation). Since each prepared bilayer had one layer with 0° orientation, we will hereafter use the term "Δθ" which refers to the difference in fiber angle between the two layers (Δθ = 0°, 22.5°, 45°, 67.5°, and 90°).

Analysis of scanning electron microscopy (SEM) images (available in the Supporting Information) revealed that the fibers, in general, were all oriented in the same direction, with minimal outliers. Additionally, the average PVAc fiber diameter was 0.81 ± 0.21 μm. A total of 150 measurements from two samples were used to calculate the average fiber diameter.

SEM images of a single layer A-SMEC showed a smooth layer of Sylgard on the surface and complete infiltration of Sylgard throughout the thickness of the fiber mat. SEM images of bilayer A-SMEC cross-sections showed the thin layer of Sylgard used for laminating the two layers. Further, the cross-sectional images showed that Sylgard provided good lamination, which is evident at the Sylgard-composite interface. It was necessary to analyze the thin layer between the bilayer system to demonstrate its minimal effect on the curling phenomenon, as this will be discussed later.

Thermal Analysis

The DSC first cooling and second heating traces for the PVAc fiber mat, neat Sylgard, and the bilayer composite are available in the Supporting Information. The measured glass transition temperatures (T_g) were found to be 42 °C and 46 °C for the PVAc fiber mat and the bilayer composite, respectively. The T_g of Sylgard was not determined from the DSC results due to instrument limitations, but it is known to be -115 °C from prior studies.[6] Our results support the previous study from our group that showed the inclusion of a PVAc fiber mat within a Sylgard matrix raises the T_g slightly, though the exact origin of this change is unknown.[9] Further, the step change in heat flow at PVAc's T_g is decreased in magnitude in the composite due to the reduced weight fraction of PVAc. Estimated gravimetrically, the PVAc comprises about 10 wt% of the bilayer composite.

Mechanical Analysis

The Young's moduli of the fiber mats, the single layers, and the bilayer A-SMECs were measured using a Linkam TST 350 tensile stress testing system. Representative stress-strain curves for the single and bilayer composites for each fiber angle are shown in **Figure 2**. **Figure 2a** shows that a higher yield stress was attained for the single layer A-SMEC with a fiber orientation of $\theta = 0°$. In general, the yield stress decreased as the fiber orientation increased (from $\theta = 0°$ to $\theta = 90°$) as a result of the reduced capacity of the fibers to bear the

load when $\theta \neq 0°$. A similar trend was observed in the neat PVAc fiber mats (stress-strain curves for the PVAc fiber mats are available in the Supporting Information). Notably, the maximum stress that was achieved for the single layer A-SMEC was lower when compared to its fiber mat state. It is postulated that this decrease is due to the decrease in fiber volume fraction when Sylgard was infiltrated due to the increase in spacing between the anisotropic fibers. **Figure 2b** shows representative stress-strain curves for the bilayer A-SMEC system and reveals that the yield stress did not show a clear dependence of fiber orientation. However, the bilayer A-SMECs with $\Delta\theta = 0°$ and 22.5° exhibited the highest yield stresses, suggesting, again, that higher stresses are achieved when fibers are oriented in, or close to, the direction of loading.

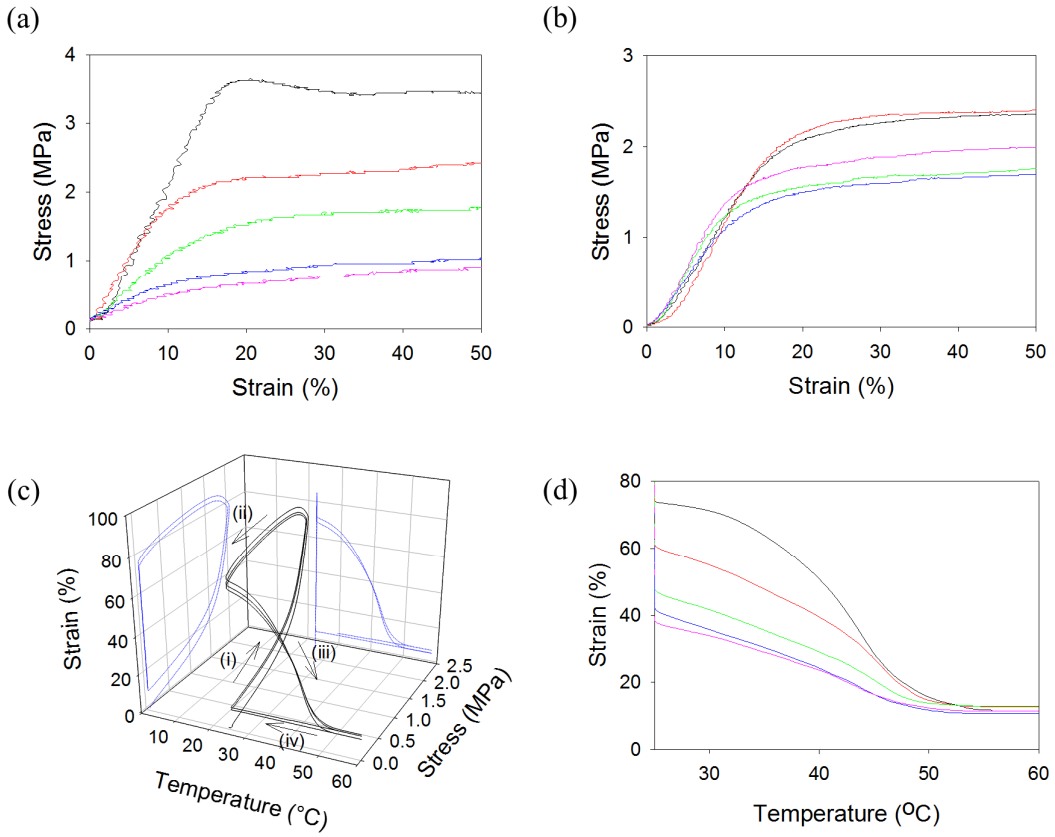

Figure 2. Representative stress-strain curves for (a) single-layer composites and (b) bilayer composites with fiber orientations (θ or $\Delta\theta$) of 0° (black), 22.5° (red), 45° (green), 67.5° (blue), and 90° (pink). Noise in (a) is evident due to the small thicknesses of the single layer A-SMECs and the limited resolution of the Linkam system. Stress-strain curves showing the strain-to-failures are available in the Supporting Information. (c) Reversible plasticity shape memory (RPSM) 3D plot of 0° single-layer A-SMEC. Projection of cycles onto strain vs. stess and strain vs. temperature planes are shown. Samples were loaded at RT (i), unloaded at

RT for fixing (ii), heated to 60 °C for recovery (iii), and cooled to RT (iv). (d) RPSM recovery of single-layer A-SMECs with fiber orientations of 0° (black), 22.5° (red), 45° (green), 67.5° (blue), and 90° (pink). The strain at 25 °C is the fixed strain in the A-SMEC after deformation to 75 % strain.

Examination of the initial slopes of the stress-strain curves shows that the Young's moduli of the PVAc fiber mats and single layer A-SMECs decreased as θ increased (a table containing the average Young's moduli is available in the Supporting Information). For θ = 0°, the fibers are aligned in the direction of loading and bear the entire load, providing a relatively high stiffness to the fiber mat. However, for θ = 90°, the fibers are initially perpendicular to the loading direction and are being pulled apart from each other. Therefore, the fibers bear little load, decreasing the stiffness of the overall material.[9] The introduction of the elastomeric Sylgard, with an average Young's modulus of 0.7 MPa, greatly altered the mechanical properties of the electrospun PVAc fiber mats, reducing the Young's modulus by an order of magnitude. While the fiber mats featured Young's moduli in the range of 20 - 200 MPa, the single layer A-SMECs featured Young's moduli in the range of 3 - 30 MPa. As stated above, this decrease in mechanical properties is postulated to be due to the decrease in fiber volume fraction in the material because of significant swelling from the Sylgard intake into the fiber mat. The Young's moduli for the bilayer system did not have a clear dependence on Δθ, and a narrow range of moduli was observed. The bilayer A-SMECs with Δθ = 0° and 22.5° had the highest moduli at ca. 17 MPa and the bilayer A-SMEC with Δθ = 45° had the lowest modulus at 11 MPa. The lack of dependence on Δθ may be explained by the complexity of the bilayer system, which will not be explored in the scope of the present study. In comparing the two composite systems, it was found that the single and bilayer A-SMECs have Young's moduli of the same magnitude; the single and bilayer A-SMECs have similar stress-strain behaviors during loading, but further investigation was beyond our present scope.

Reversible Plasticity Shape Memory of Single Layer Composites

A reversible plasticity SM (RPSM) method was used to characterize the SM properties of the single layer A-SMECs as a function of angle (θ) relative to the direction of uni-axial stretching. A representative 3D stress-temperature-strain plot is shown in **Figure 2c** for the single layer A-SMEC with θ = 0°. Upon uni-axially stretching at RT, which is below the T_g of the PVAc fibers but above the T_g of the Sylgard, each specimen was deformed both elastically and plastically. This deformation is thought to assist in further orienting the anisotropic fibers and drives the chain conformation of both phases to a lower entropy state. Upon unloading, the temporarily fixed deformation was measured and each specimen was heated to 60 °C to observe the shape recovery and then cooled to RT to complete the RPSM cycle.

The recovery curves for the single layer A-SMECs with various fiber orientations are shown in **Figure 2d**. Each strain level observed at 25 °C (before heating) represents the level of strain fixed for the different A-SMEC orientations following deformation to 75% strain. The fixing ratio (R_f) (Eq. 1) was affected by plastic deformation of PVAc fibers below their T_g and also depended on the θ relative to the direction of uni-axial stretching. As θ increased from 0° to 90°, R_f decreased from 85 % to 50 % under the effect of elastic contractile force of the Sylgard matrix that became dominant over the orientated fibers' plastic deformation, following a trend also seen by Rodriguez et al. for a conventional shape memory thermal cycle.[9] Sylgard is an elastomeric rubber, while PVAc is glassy. Below PVAc's T_g, the fibers oppose the elastomeric matrix from contracting . The ability to resist contraction, however, diminishes as the fiber oriention is increased away from the load direction. The recovery ratio, R_r (Eq. 2), for all single layer A-SMECs were found to be higher than 96% for cycles two and three but as low as 78 to 88% for cycle one. Sylgard was tested as a control, and its fixing ratio was close to 0% due to its elastic nature. Therefore, the recovery ratio, as conventionally

defined, could not be calculated. The 3D stress-temperature-strain plots for all single layer A-SMECs and tabulated R_f and R_r are available in the Supporting Information

Mechanically Programmed Shape Change of Bilayer A-SMECs

Curvature in bilayer systems arises when a mismatch of strain between the two layers exists. For example, in substrate/coating systems a strain mismatch often arises when subjected to a temperature change due to differences in the thermal expansion coefficients of the substrate and coating,[27] resulting in bending of the bilayer system. In the A-SMEC bilayer systems reported of the present study, a mismatch in strain arises from the difference in the strain fixing (or, conversely, elastic recovery) of each layer, resulting in bending of the bilayer. **Scheme 1** demonstrates the effect of fiber orientation on the behavior of the single and bilayer A-SMECs subjected to tensile deformation. In-plane rotation of the bilayers with different fiber orientations leads to helix formation.

Samples of varying $\Delta\theta$ were stretched to varying levels of strain: 40, 50, 75, or 100%/ Remarkably, upon unclamping, a non-affine shape change occurred, as the samples changed from flat strips to coils or twisted coils. Attaining a similar shape change in typical SMPs requires both thermal control and complex manipulation with the aid of a mandrel. Thus, tensile mechanical programming at RT drastically simplifies the programming process. A representative set of images of curled bilayer A-SMECs stretched to 75% strain are shown in **Figure 3** (Images of samples stretched to 40, 50, and 100% strain are available in the Supporting Information), revealing the complex, 3D shapes prepared from flat films with this accelerated shape forming processe. For $\Delta\theta = 0°$, where the relative angle between the fibers and the stretching direction was 0° for both layers, the fixing ratios were the same. Therefore, there was no mismatch between the layers, and the sample remained straight post-stretching. On the other hand, for $\Delta\theta \neq 0°$, the fixing ratio of each layer was different since there was a mismatch between the fixed lengths, leading to a curled state. In studying the images in

Figure 3, it can be seen qualitatively that the pitch and radius of curvature tend to decrease with increasing Δθ.

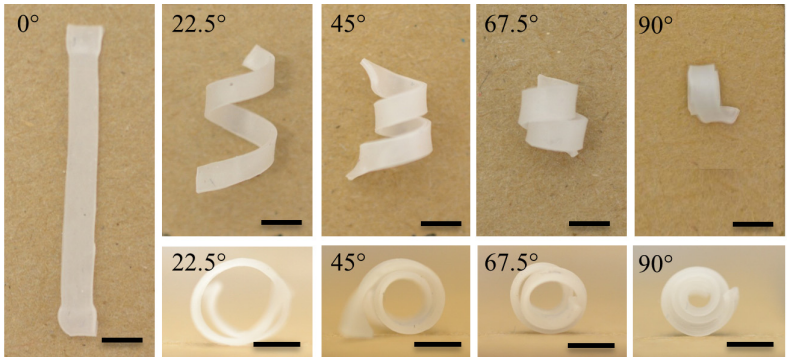

Figure 3. Representative images of curled bilayer A-SMECs stretched to 75% strain indicating the pitch in the top row and the radius of curvature in the bottom row. Δθ is indicated on top left corner of each image. Scale bars represent 4 mm.

After deforming four different samples to 40, 50, 75, and 100% strain, the curling was quantified by measuring the radius of curvature and pitch. The circles and lines drawn in **Figure 4a** demonstrate how the measurements of radius of curvature and pitch were obtained using ImageJ software. In our analysis, it was realized that the curvature followed a simple but significant dependence on sample thickness (thinner samples curling proportionally more); therefore, all curvature radii were normalized by the total thickness in making comparisons and observing trends. In particular, the measured radius of curvature for each sample was divided by the total bilayer thickness for each specimen, the reciprocal being reported as the normalized curvature.

Figure 4b and 4c show the results for the pitch and normalized curvature as a function of fiber orientation. We observed that the pitch decreased with increasing Δθ while the normalized curvature increased with increasing Δθ. In other words, a tighter curl was achieved when the difference in fiber orientation between the layers was increased. Increasing programming strain was observed to increase the normalized curvature asymptotically, while decreasing the pitch for all Δθ. (We note that no curvature measurements were reported for Δθ = 0° since the samples remained in a flat state, while quantitative pitch analysis for the Δθ = 22.5° at 40% strain was not reported because at lower

strain the specimens made less than one complete curl. Therefore, the distance between consecutive peaks or troughs could not be measured.) Upon heating above the T_g of the fiber phase (PVAc), the mechanically programmed bilayers quickly and completely returned to their equilibrium, flat state (Scheme 1). Videos of the mechanical programming and shape recovery are available in Supporting Information.

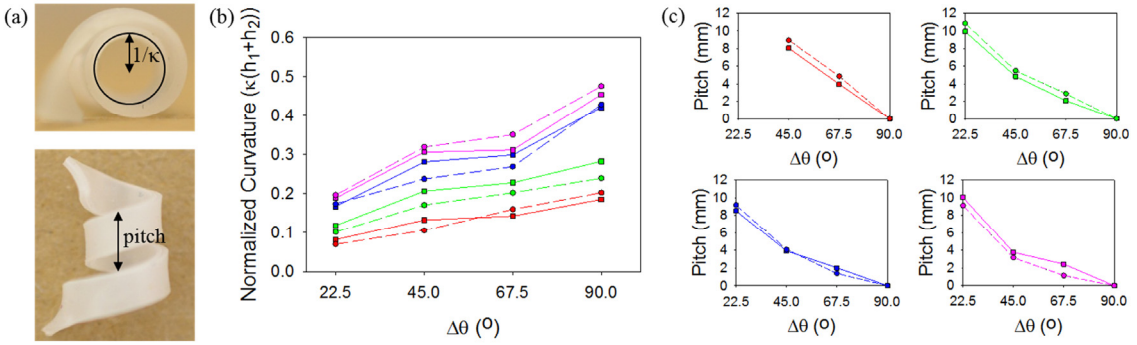

Figure 4. (a) Representation of the method used to experimentally measure the curvature and pitch. (b) and (c) Comparison of the experimental (—■—) and theoretical (--●--) results for curvature and pitch, respectively, as a function of Δθ for bilayer A-SMECs stretched to 40 (red), 50 (green), 75 (blue) and 100 (pink) % strain.

Comparing Theoretical Predictions of Curvature and Pitch to Experimental Results

The observation of non-affine shape programming is very different from the phenomena demonstrated in most SMPs to date where a programmed shape shows affinity to the applied mechanical deformation. For example, an applied stretching deformation programs the SMP into a stretched shape. The non-affine shape change opens a new design space for a wide range of potential applications, but at the same time imposes challenges on how to achieve desired shape change. Here, we developed a mechanical model to predict the shape change. To determine how well our model (described in the Experimental section and Supporting Information) predicts curvature and pitch for mechanically programmed A-SMEC bilayers, we compared theoretically predicted values to those measured experimentally. First, model parameters were calibrated by fitting measured stress-strain curves of A-SMECs with fibers oriented at 90° and 0° as shown in **Figure S7** in the Supporting Information. By fitting the

stress-strain curve of an A-SMEC with a fiber orientation of 90°, the temperature-dependent modulus of the matrix can be extracted. Likewise by fitting the stress-strain curve of an A-SMEC with a fiber orientation of 0°, the elastic modulus and viscosity-associated material parameters of the PVAc fibers can be extracted. Upon obtaining these material parameters, the predicted stress-strain behavior of an A-SMEC with a fiber orientation of 22.5° agrees well with measured values, as is shown in **Figure S7**. The calibrated material parameters are listed in **Table S2** in the Supporting Information.

Figure 4b shows the comparison of the experimentally measured and theoretically calculated normalized curvature as functions of $\Delta\theta$ and strain. In both experiment and theory, calculated normalized curvature increased with increasing $\Delta\theta$. As the deformation strain increased, the curvature also increased, as is seen in vertical shifts between plots in Figure 4b. Theoretical predictions for pitch were also compared to experimental values. **Figure 4c** shows the comparison of experimental and theoretical results for pitch as a function of $\Delta\theta$ for bilayer A-SMECs stretched to different strains. In agreement with the experimental results, as $\Delta\theta$ increases, the pitch decreases. This trend was observed for all strains tested. The theoretical dependence of pitch on strain also matched to experimental results; with increasing strain, there was a decrease in pitch. When the fiber angle in the non-0° layer was 90°, the pitch for all strains was zero and the theoretical predictions overlapped with the experimental results. Theoretical predictions of the curvature and pitch agree well with experimentally measured values. From these experiments and theoretical simulations, we deduce that predictable geometry of curling can be achieved via mechanical programming of bilayer A-SMECs with different fiber angles.

Complex Shapes

Given the observed dependence of curling on the fiber orientation, we realized a potential for the construction of interesting 3D structures simply by cutting shapes out of a bilayer A-SMEC sheet using lines selected strategically relative to the anisotropy directions. Using a

sheet with $\Delta\theta = 90°$, a 3-pronged "propeller", a triangle, and a circle were cut from the mat. The orientation of cutting for each shape is shown in **Figure 5a.** Each prong of the propeller and each side of the triangle was stretched individually. The circle was stretched in small segments, working around the shape. The arrows in **Figure 5a** indicate stretching for each shape. Images of the shapes prior to deformation and of the 3D structures obtained after the mechanically programmed shape change are shown in **Figures 5b and 5c**, respectively. For the propeller, the prong with fiber orientations of 0°/90° (with respect to the stretching direction), curled after deformation with no pitch. This is consistent with the results reported previously. The two prongs cut diagonally across the mat have fiber orientations of +60°/-30° and -60°/+30° relative to the axes of the prongs. Here, a sign convention was adopted since one layer is no longer in the 0° direction. After deformation, these two prongs curled and formed helicoids due to the difference in recovery between the two layers. Furthermore, each helicoid is roughly a mirror image of the other due to the opposite signs in the fiber orientations. For the triangle, one side had fiber orientations of 0°/90°. Since an equilateral triangle was cut, the other two sides, again, had fiber orientations of +60°/-30° and -60°/+30°. After deformation, all sides curled, but were constrained at the ends due to the connection to the other sides of the triangle. The 0°/90° side formed an arch shape, and the +60°/-30° and -60°/+30°, which would have formed helicoids if unconstrained, curled back towards the third side. Finally, a circle was cut from the bilayer A-SMEC with $\Delta\theta = 90°$. While a variety of fiber orientations were present, constraint imposed by the continuous circular geometry defined the overall shape change. After deformation, the circle formed a saddle-like structure, with arches forming through the segments where the tangent to the circle is parallel to one of the fiber orientations (and perpendicular to the other). The concavity of the arch depended on the position of the layer with a relative fiber orientation of 90°. As explained previously, due to the lower fixing of a 90° layer compared to a 0° layer, the bilayer curls towards the 90° ply. All 3D shapes recovered to their flat forms upon heating above the T_g of PVAc and the

process of mechanical programming repeated. It is clear that many interesting 3D structures can be obtained by adjusting the initial cut shape and varying the fiber orientations of the layers.

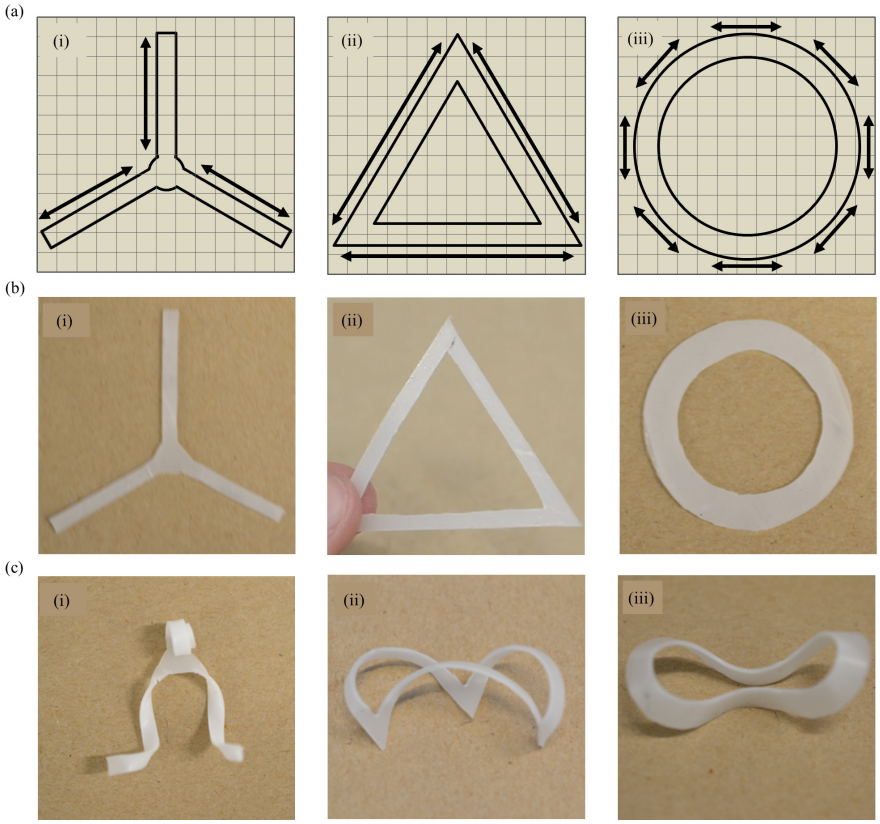

Figure 5. 3D structures obtained from cutting shapes out of a bilayer A-SMEC sheet with $\Delta\theta = 90°$. Images show (a) a schematic of the cutting (solid lines) and stretching (arrows) orientations, (b) the shapes prior to deformation, and (c) the 3D structures obtained after mechanically activated shape change for (i) the propeller, (ii) triangle, and (iii) circle.

Conclusions

We have successfully introduced unique anisotropic SM composites that can be mechanically programmed from 2D films to 3D complex shapes at RT. Achieving the non-affine shape change with a simple tensile programming step is atypical for SMPs, which normally require significant manipulation and thermal control to achieve such a drastic shape change. This unique characteristic can be used for fabrication of composites with predictable SM behavior that target specific biomedical and aerospace applications. Furthermore, the programmed 3D shapes can be triggered to return to their equilibrium, flat shape by heating through the T_g of

the fiber phase (here PVAc), adding the advantages of reversibility and repetitive programming. Results showed dependence of Young's modulus on fiber orientation for anisotropic PVAc fibers and for single and bilayer A-SMEC systems. RPSM was used to quantify the dependence of fixing and recovery on the fiber angle for single layer composites. Due to the dependence of fixing on the fiber orientation, mechanically programmed bilayer A-SMECs curled, and the pitch and radius curvature were analyzed qualitatively and quantitatively for all fiber orientations deformed to various strains. The radius of curvature and pitch decreased in response to a mismatch in strain caused by an increase in $\Delta\theta$. A simple theoretical model was developed to predict the observed dependence of shape fixity, curvature, and pitch on the fiber orientation and applied strains and showed good agreement with experimental data. Future research will develop a more sophisticated model that can capture the distribution of stress in the laminate during deformation. Such a model will help evaluate the possibility of delamination, which will be an important consideration for real applications of the materials. Additionally, future research is needed in the area of multilayered composites extending beyond just two layers, the additional complexity likely enabling even more complex structures via mechanical programming. We anticipate that these mechanically programmed shape memory elastomeric composites of the present work will find use in aerospace applications, packaging, biophysical research,[28] and such medical devices as stents and catheters.[29]

Acknowledgements

PTM and HJQ acknowledge funding under NSF CMMI-1334658/1441375 and NSF EFRI-1435452.

Notes and references

[a]*These authors contributed equally to this work.*
[b]*Syracuse Biomaterials Institute and Biomedical and Chemical Engineering, Syracuse University, Syracuse, NY, 13244, USA*
E-mail: ptmather@syr.edu

[c]The George W. Woodruff School of Mechanical Engineering, Georgia Institute of Technology, Atlanta, GA 30332, USA

†Electronic Supplementary Information (ESI) available: SEM micrographs; DSC thermograms; stress-strain curves; tabulated mechanical properties; Reversible Plasticity Shape Memory (RPSM) curves; tabulated RPSM characteristics; photographs of mechanically programmed materials; Videos of mechanical programming; Comparison of model and experiment; Derivation of consitutive relations; Solution to theoretical model. See DOI: 10.1039/b000000x/

1 Mendez, J.; Annamalai, P. K.; Eichhorn, S. J.; Rusli, R.; Rowan, S. J.; Foster, E. J.; Weder, C., *Macromolecules* 2011**, 44**, 6827-6835.
2 Jiang, H. Y.; Kelch, S.; Lendlein, A., *Advanced Materials* 2006**, 18**, 1471-1475.
3 Ge, Q.; Luo, X.; Iversen, C. B.; Mather, P. T.; Dunn, M. L.; Qi, H. J., *Soft Matter* 2013**, 9**, 2212-2223.
4 Liu, C.; Qin, H.; Mather, P. T., *Journal of Materials Chemistry* 2007**, 17**, 1543-1558.
5 Luo, X.; Mather, P. T., *Current Opinion in Chemical Engineering* 2013**, 2**, 103-111.
6 Luo, X.; Mather, P. T., *Macromolecules* 2009**, 42**, 7251-7253.
7 Burt, T. M.; Jordan, A. M.; Korley, L. T. J., *ACS Applied Materials & Interfaces* 2012**, 4**, 5155-5161.
8 Li, Y.; Iwakura, Y.; Nakayama, K.; Shimizu, H., *Composites Science and Technology* 2007**, 67**, 2886-2891.
9 Rodriguez, E. D.; Weed, D. C.; Mather, P. T., *Macromolecular Chemistry and Physics* 2013**, 214**, 1247-1257.
10 Cao, D.; Liu, W.; Wei, X.; Cui, L.; Cao, Y., *Tissue Engineering* 2006**, 12**, 1369-1377.
11 Ayres, C.; Bowlin, G. L.; Henderson, S. C.; Taylor, L.; Shultz, J.; Alexander, J.; Telemeco, T. A.; Simpson, D. G., *Biomaterials* 2006**, 27**, 5524-5534.
12 Valderrábano, M., *Progress in Biophysics and Molecular Biology* 2007**, 94**, 144-168.
13 Li, Z.; Guan, J., *Polymers* 2011**, 3**, 740-761.
14 Engelmayr, G. C., Jr.; Cheng, M.; Bettinger, C. J.; Borenstein, J. T.; Langer, R.; Freed, L. E., *Nature Materials* 2008**, 7**, 1003-1010.
15 Jean, A.; Engelmayr, G. C., Jr., *Journal of Biomechanics* 2010**, 43**, 3035-3043.
16 Godinho, M. H.; Canejo, J. P.; Feio, G.; Terentjev, E. M., *Soft Matter* 2010**, 6**, 5965-5970.
17 Armon, S.; Efrati, E.; Kupferman, R.; Sharon, E., *Science* 2011**, 333**, 1726-1730.
18 Matsuyama, H.; Berghmans, S.; Lloyd, D. R., *Polymer* 1999**, 40**, 2289-2301.
19 Burke, K. A.; Mather, P. T., *Journal of Materials Chemistry* 2010**, 20**, 3449-3457.
20 Jeong, K.-U.; Jang, J.-H.; Kim, D.-Y.; Nah, C.; Lee, J. H.; Lee, M.-H.; Sun, H.-J.; Wang, C.-L.; Cheng, S. Z. D.; Thomas, E. L., *Journal of Materials Chemistry* 2011**, 21**, 6824-6830.
21 Kohlmeyer, R. R.; Buskohl, P. R.; Deneault, J. R.; Durstock, M. F.; Vaia, R. A.; Chen, J., *Advanced Materials* 2014**, 26**, 8114-8119.
22 Huang, Z.-M.; Zhang, Y. Z.; Kotaki, M.; Ramakrishna, S., *Composites Science and Technology* 2003**, 63**, 2223-2253.
23 Qi, G.; Conner, K. D.; Qi, H. J.; Martin, L. D., *Smart Materials and Structures* 2014**, 23**, 094007.
24 Westbrook, K. K.; Kao, P. H.; Castro, F.; Ding, Y.; Jerry Qi, H., *Mechanics of Materials* 2011**, 43**, 853-869.
25 Williams, M. L.; Landel, R. F.; Ferry, J. D., *Journal of the American Chemical Society* 1955**, 77**, 3701-3707.
26 Di Marzio, E. A.; Yang, A. J. M., *Journal of Research of the National Institute of Standards and Technology* 1997**, 102**, 135.
27 Clyne, T. W., *Key Engineering Materials* 1995**, 116-117**, 307-330.

28 Tseng, L.-F.; Mather, P. T.; Henderson, J. H., *Acta Biomaterialia* 2013**, 9**, 8790-8801.
29 Lendlein, A.; Langer, R., *Science* 2002**, 296**, 1673-1676.

Mechanically Programmed Shape Change in Laminated Elastomeric Composites